Structures 60 (2024) 105880

Contents lists available at ScienceDirect

Structures

journal homepage: www.elsevier.com/locate/structures

A comprehensive evaluation of the vibration control approach of the multi-layer sandwich composite piezoelectric micro-beam using higher-order elasticity theory and surface energy

Mehrdad Soltani [a,b], Javad Jafari Fesharaki [a,b,*], Seyed Ali Galehdari [a,b], Rasoul Tarkesh Esfahani [a,b], Mohamad Shahgholi [a,b]

[a] Department of Mechanical Engineering, Najafabad Branch, Islamic Azad University, Najafabad, Iran
[b] Modern Manufacturing Technologies Research Center, Najafabad Branch, Islamic Azad University, Najafabad, Iran

ARTICLE INFO

Keywords:
Active vibration control
Multi-layer sandwich composite piezoelectric micro beam
Higher-order theories
GDQM
Vibration suppression

ABSTRACT

The present study is devoted to investigate the comprehensive study of vibration control of multi-layer sandwich micro beam made of piezoelectric materials. The analysis considers the influences of all parameters, such as strain gradient theories and surface effects. To assess the efficacy of control measures for the multi-layer sandwich composite piezoelectric micro-beam and to obtain the corresponding mechanical properties, the Hamiltonian approach and the generalized differential quadrature (GDQ) method were employed in the discretized solution. The governing partial differential equation (PDE) of motion is converted into a set of ordinary differential equations (ODE) employing the GDQ method. Additionally, the researchers design different controllers to investigate the tracking performance and vibration suppression of the system. The results indicate that the electrical voltage of the piezoelectric layer plays a key role in designing a controller for multi-layer sandwich composite piezoelectric micro-beams. The findings of this study suggest that the Linear Quadratic Integral (LQI) control scheme is much more effective in terms of vibration control and tracking characteristics, as well as feedback damping factors, within the allowable voltage of the piezoelectric actuator.

1. Introduction

Nowadays, nano and microstructures integrated with "Smart" materials play an outstanding role in the engineering area. Many micro and nano systems cannot be properly evaluated without analyzing their structure. In addition to studies dealing with nanosystem designations, there are many studies investigating the vibrational behavior of micro and nanosystems [1–5]. With the emergence of recent breakthroughs in the field of micro/nano-fabrication, there has been a significant surge in interest surrounding micro- or nano-sized structures and their potential applications in the development of micro/nano-electromechanical systems (MEMS/NEMS) [4,6–8]. Notably, carbon nanotubes, micro actuators, microfilms, nanowires, atomic force microscope, nano-wire-fabricated nano-tweezers and nano-switches have garnered considerable attention as highly promising miniature systems that hold great potential within the realms of bio-engineering, medicine, electronics, nanoscale fabrications, sensing, mass-detecting, and other related fields [1,9–13]. Nano and microtechnology, promises new possibilities for developing stiffer, lighter, and smarter structures [14,15]. It also, can be improved the properties of piezoelectric materials [16–18]. The author considers sandwich structures integrated with smart piezoelectric material and exposed to multiple fields loads to be a new and attractive analysis of fine structures. These structures can be used as actuators and sensors and for micro-technical issues. A comprehensive literature search can be guaranteed the necessity of the present research [2,19,20]. In addition, Korayam et al. analyzed nonlinear frequency behavior, in separate research [21]. Khaniki and Hashemi studied the dynamic behavior of a multi-layered viscoelastic nanobeam system embedded in a viscoelastic medium with a moving nanoparticle [22]. The researchers utilized the Winkler elastic foundation beam technique in order to effectively represent the interlayer coupling and small-scale effects, while simultaneously incorporating the modified couple stress theory. Through the implementation of Hamilton's principle, the equations of motion were simulated and subsequently solved to determine the solution process. Hashemi et al. [23] investigated the dynamic behavior of multi-layered viscoelastic

* Corresponding author at: Department of Mechanical Engineering, Najafabad Branch, Islamic Azad University, Najafabad, Iran.
E-mail address: jjafari.f@gmail.com (J.J. Fesharaki).

https://doi.org/10.1016/j.istruc.2024.105880
Received 17 September 2023; Received in revised form 30 December 2023; Accepted 8 January 2024

nanobeams resting on a viscoelastic medium with a moving nanoparticle. They used Eringens nonlocal theory is used to model the small-scale effects. Their study examines the effects of various factors such as the nonlocal parameter, stiffness and damping parameter of the medium, internal damping parameter, and the number of layers on the trajectory of the nanoparticle passing through.

Arshid et al. [24] investigated vibrational behavior of a functionally graded graphene nanoplatelets-reinforced porous nanocomposite (FG GNPs-RPN) annular microplate with piezoelectric coverings. They concluded that incorporating GNPs into the system results in a notable increase in frequencies, with an enhancement of approximately 20–28%. Conversely, elevating the porosity levels to a maximum of seventy percent yields a reduction in frequencies, with a decrease of about 8–15%. Soleimani-Javid et al. [24] presented the free vibrational behaviors of functionally graded saturated porous micro cylindrical shells with two nanocomposite skis. Arshid et al. [25] developed vibrational behavior of the three-layered sandwich microplate containing functionally graded (FG) porous materials as core and piezoelectric nanocomposite materials as face sheets subjected to electric field resting on Pasternak foundation.

Kabir et al. [26] employed piezoelectric micro-electromechanical systems (MEMS) acoustic emission sensors design to discover elastic waves. Wang et al. [27] developed the vibration properties of multilayer plates by taking the influence of surface energy into account. In their study, a nonlinear model was used to investigate the consequences of large amplitude oscillations. Also, a high-amplitude free-oscillating electrically driven nanobeam was presented by Wang et al. [28].

Chaudhari and Lal investigated the nonlinear free vibration behavior of elastically supported carbon nanotube reinforced composite beam subjected to thermal loading. They employed higher order shear deformation theory with von-Karman nonlinear kinematics model the through Hamilton principle to establish the integral form of the equation of motion of the beam [29–31]. Zheng et al. used Reddy's third-order shear deformation theory and nonlocal elasticity theory, to present a nonlinear bending model of the nonlocal three-layer magneto--electro-elastic laminated nanobeam resting on elastic foundation. Their results discussed the effects of foundation parameters, nonlocal parameter, external electric voltage and external magnetic potential on bending behaviors model [32].

It will become even more complicated matters by using the experimental strategies for assessing the mechanical behavior of MEMS and NEMS are normally very time-ingesting and costly. Hence, numerical simulations, primarily based entirely on the mathematical theory of continuum elasticity, have been significantly completed to manage MEMS / NEMS and analyze mechanical behavior [21,33,34]. In addition to many studies for calculating the mechanical properties of these MEMS / NEMS systems, there are other studies focused primarily on determining stability, vibration, and volume expansion conditions [35,36]. Meanwhile, many researchers are suggesting various methods to solve engineering problems. However, without paying too much attention to the MEMS/NEMS control, the results are scattered, insufficient to determine a unique set of material parameters [37,38]. The free and forced vibrations of a three-dimensional nonplanar nanobeam with initial geometric imperfection using nonlocal strain gradient theory, presented by Wu et al. [39]. They employed Hamilton's principle and GDQM to derive and discretize the equations, respectively. A robust optimization approach for controlling and suppressing nonlinear beam oscillations has been extended by Moradi et al. [40]. They used Hamilton's principle to derive a non-linear differential equation for beam motion and utilized fuzzy controller circuits to reduce forced vibration. Numerical simulation to explain the effect of adaptive boundary control was Nojoumian et al. [41]. They studied vibration control and reimbursement of the system parametric uncertainties for a micro cantilever beam based on strain gradient theory (SGT). Quang et al. [42] to investigate the active vibration control of functionally graded material (FGM) plates integrated with piezoelectric layers. Moreover, Ghorbanpour Arani et al. [43] proposed vibration control subjected the multi-physical loads based on higher-order shear deformation theory for essentially backed boundary conditions. In their work, the utilization of generalized differential quadrature method (GDQM) has been effectively detailed for vibration control investigations of the magnetostrictive plate. Akhavan Alavi et al. [44] focused on numerical study of active control for functionally graded nanocomposite micro Reddy beam. A LQR controller was utilized to calculate beam demonstration with optimal tuning parameters. Vatankhah and Asemani conducted an assessment of the efficacy of output feedback control in relation to the piezoelectric actuation of a non-classical micro beam. This evaluation was achieved through the utilization of a Takagi-Sugeno fuzzy system. [45]. They employed SGT to drive the governing partial differential equation. A quadratic remarks controller to reduce the vibration of micro-scale systems primarily based on multi-moment matching criteria became designed through Vakilzadeh et al. [46]. The finite element method (FEM) was applied to model the micro-cantilever beam.

In addition, the simulation effects of making utilize of the proposed adaptation had been taken into thought as an objective of Khaje khabaz et al. [47]. They analyzed optimal control of a micro-beam included with piezoelectric layers with considering the modified couple stress theory (MCST). Their utilized linear quadratic regulator (LQR) controller to reduce the vibration amplitude of model [48].

Wang et al. investigated the kriging-based decoupled non-probability reliability-based design optimization scheme for piezoelectric PID control systems. They presented a new adaptive learning strategy which involves two stages of enrichment to improve the accuracy of the surrogate model in the region of interest [49].

The researchers have focused on the use of micro and nanostructures including the mechanical and size-dependent behavior of smart materials using higher-order elasticity theories. On the alternative hand, because of the problems in growing and fixing equations of movement to are expecting the correct conduct of complicated micro and nanostructures, little interest has been paid to vibration control. According to an analysis of earlier studies, many academics have thought about using post-processing techniques like Galerkin and GDQM to discretize the partial equation of motion. However, the majority of research in this sector focuses on simulation modeling approaches for problems because it is difficult to conduct practical tests at the micro and nano scales. Furthermore, to the authors' best knowledge there is far little attention has been paid to the vibration control simulations based on multi-layer sandwich composite piezoelectric micro beam using higher-order elasticity theory and surface energy. In addition, the main purpose of this study is to improve the concept of optimum design of the controller, and compare the controller parameters, which to the best knowledge of the authors, few analyses have examined the influence of the effective parameters of the design based on mathematical simulation. Therefore, the best technique was determined by computing metrics like LQI and LQR.

The novelty of this article is the fact that vibration control by using different methods and the comparison of the dynamic response based on different higher-order theories and surface effects has been considered simultaneously. Moreover, deriving and solving the governing equation of multi-layer sandwich composite piezoelectric micro beam using higher-order elasticity theory and surface effects is presented for the first time. In addition, no reference has been made so far in the literature on the vibration control approach of this model.

The present study is focused on the comprehensive vibration evaluation and control of multilayer composite piezoelectric microbeams using the SGT and surface effects. Hamilton's approach and GDQ method have been used to derive and solve the governing equations of motion. The various controller such as LQR and linear quadratic integral (LQI) control are investigated. The results control can be used for MEMS and NEMS to prevent resonance phenomena.

2. Methodology

In the present study, the front panel of the multilayer microbeam is made of a silicon material with a PZT4 piezoelectric layer acting as a distributed sensor and actuator [50,51]. In the event of mechanical or thermal vibration of the structure, the deformation of the model can be obtained by measuring the charge induced in the sensor layer. This can be controlled by a control algorithm that uses the strain or tension of the application [52,53]. The displacement fields of the structure are Euler-Bernoulli beam which can be defined as below:

$$U_1(x,y,z) = -Z\frac{\partial w(X,t)}{\partial X}$$

$$U_2(x,y,z) = 0$$

$$U_3(x,y,z) = w(X,t) \tag{1}$$

where U and w are the displacement components along different directions and transverse displacement, respectively.

2.1. constitutive equations of model

The potential strain energy without surface effect is extracted as [54,55]:

$$U = \int_{\Omega} (\sigma_{ij}e_{ij} + P_i\gamma_i + \tau_{ijk}^{(1)}\eta_{ijk}^{(1)} + m_{ij}x_{ij} - D_iE_i)dV \tag{2}$$

Where $\sigma_{ij}, \varepsilon_{ij}, \gamma_i, m_{ij}\ \eta_{ijk}^{(1)}, E_i$ and x_{ij} denote Cauchy stress tensor, strain tensor, dilation gradient tensor, deviatoric part of couple stress tensor, the symmetric rotation gradient tensor, the electric field and the deviatoric stretch gradient tensor, respectively [56,57]. In addition, p_i and $\tau_{ijk}^{(1)}$are higher order stresses. The strain–displacement relations of the structure are considered:

$$\varepsilon_{11} = -Z\frac{\partial^2 w}{\partial x^2} \tag{3}$$

The stress–strain relations of the bulk and piezoelectric layers can be derived as:

$$\sigma_{11}^{B} = -EZ\frac{\partial^2 w}{\partial x^2} \tag{4}$$

$$\sigma_{11}^{P} = C_{11}^{P}\varepsilon_{11} - e_{31}E_3^{P} \tag{5}$$

In which C_{ij}^{P}, e_{ij} and E $(i,j = 1,2,3)$ denote the piezoelectric elastic moduli, piezoelectric coefficients and Young's modulus, respectively.

The constitutive relation of the piezoelectric are calculated by [58]:

$$D_3 = e_{31}\varepsilon_{11} + \epsilon_{33}E_3^{P} \tag{6}$$

In which D_i and ϵ_{ij} $(i,j = 1,2,3)$ are electrical displacement and the dielectric permittivity constant, respectively. The electric potential for top and bottom layers of piezoelectric materials are defined as [59]:

$$\Phi^{(a)}(x,z,t) = -\cos(\beta z)\phi^{(a)}(x,t) + \frac{2zV_0}{h^{(a)}} \tag{7}$$

$$\Phi^{(s)}(x,z,t) = -\cos(\beta z)\phi^{(s)}(x,t) \tag{8}$$

$\beta = \pi/h^{(p)}$ and V_0 is the external voltage, which is subjected to the actuator layer. It is worth mentioning that the piezoelectric layers sensors and actuators are indicated by the superscript letter's "s", "a". In addition, "B" and "P" symbols show the bulk and piezoelectric layer related equations [60]:

$$E_3^{(a)} = \frac{\partial\Phi^{(a)}}{\partial z} = \beta\sin(\beta z)\phi^{(a)}(x,t) - \frac{2V_0}{h^{(a)}} \tag{9}$$

$$E_3^{(s)} = \frac{\partial\Phi^{(s)}}{\partial z} = \beta\sin(\beta z)\phi^{(s)}(x,t)$$

In addition, according to the SGT which is introduced in Appendix A, the three-size dependent material length scales are obtained as:

$$\chi_{12} = \chi_{21} = -\frac{1}{2}\frac{\partial^2 w}{\partial x^2} \tag{10}$$

$$\gamma_1 = \varepsilon_{11,1} = -Z\frac{\partial^3 w}{\partial x^3} \tag{11}$$

$$\gamma_3 = \varepsilon_{11,3} = -\frac{\partial^2 w}{\partial x^2}$$

$$\eta_{113}^{(1)} = \eta_{131}^{(1)} = \eta_{311}^{(1)} = -\frac{4}{15}\frac{\partial^2 w}{\partial x^2} \tag{12}$$

$$\eta_{111}^{(1)} = -\frac{2}{5}Z\frac{\partial^3 w}{\partial x^3}$$

$$\eta_{333}^{(1)} = \frac{1}{5}\frac{\partial^2 w}{\partial x^2}$$

$$\eta_{223}^{(1)} = \eta_{232}^{(1)} = \eta_{322}^{(1)} = \frac{1}{15}\frac{\partial^2 w}{\partial x^2}$$

$$\eta_{122}^{(1)} = \eta_{212}^{(1)} = \eta_{221}^{(1)} = \eta_{133}^{(1)} = \eta_{331}^{(1)} = \eta_{313}^{(1)} = \frac{1}{5}Z\frac{\partial^3 w}{\partial x^3}$$

The higher-order stresses defined as [60]:

$$m_{12}^{B} = m_{21}^{B} = -\mu l_2^2\frac{\partial^2 w}{\partial x^2} \tag{13}$$

$$m_{12}^{P} = m_{21}^{P} = -\mu l_2^2\frac{\partial^2 w}{\partial x^2}$$

$$p_1^{B} = -2\mu l_0^2 Z\frac{\partial^3 w}{\partial x^3} \tag{14}$$

$$p_3^{B} = -2\mu l_0^2\frac{\partial^2 w}{\partial x^2}$$

$$p_1^{P} = -2\mu l_0^2 Z\frac{\partial^3 w}{\partial x^3} \tag{15}$$

$$p_3^{P} = -2\mu l_0^2\frac{\partial^2 w}{\partial x^2}$$

$$\tau_{113}^{B(1)} = \tau_{131}^{B(1)} = \tau_{311}^{B(1)} = -\frac{8}{15}\mu l_1^2\frac{\partial^2 w}{\partial x^2}$$

$$\tau_{111}^{B(1)} = -\frac{4}{5}\mu l_1^2 Z\frac{\partial^3 w}{\partial x^3}$$

$$\tau_{333}^{B(1)} = \frac{2}{5}\mu l_1^2\frac{\partial^2 w}{\partial x^2}$$

$$\tau_{223}^{B(1)} = \tau_{232}^{B(1)} = \tau_{322}^{B(1)} = \frac{2}{15}\mu l_1^2\frac{\partial^2 w}{\partial x^2}$$

$$\tau_{122}^{B(1)} = \tau_{212}^{B(1)} = \tau_{221}^{B(1)} = \tau_{133}^{B(1)} = \tau_{331}^{B(1)} = \tau_{313}^{B(1)} = \frac{2}{5}\mu l_1^2 Z\frac{\partial^3 w}{\partial x^3} \tag{16}$$

$$\tau_{122}^{P(1)} = \tau_{212}^{P(1)} = \tau_{221}^{P(1)} = \tau_{133}^{P(1)} = \tau_{331}^{P(1)} = \tau_{313}^{P(1)} = \frac{2}{5}\mu l_1^2 Z\frac{\partial^3 w}{\partial x^3}$$

$$\tau_{223}^{P(1)} = \tau_{232}^{P(1)} = \tau_{322}^{P(1)} = \frac{2}{15}\mu l_1^2\frac{\partial^2 w}{\partial x^2}$$

$$\tau_{333}^{P(1)} = \frac{2}{5}\mu l_1^2 \frac{\partial^2 w}{\partial x^2}$$

$$\tau_{113}^{P(1)} = \tau_{131}^{P(1)} = \tau_{311}^{P(1)} = -\frac{8}{15}\mu l_1^2 \frac{\partial^2 w}{\partial x^2}$$

$$\tau_{111}^{P(1)} = -\frac{4}{5}\mu l_1^2 Z \frac{\partial^3 w}{\partial x^3} \tag{17}$$

2.2. Fundamental relation of surface layers

The potential strain energy in the structure without surface effect is extracted as follows [61]:

$$U_s = \frac{1}{2}\int_0^L \oint_{\partial A} (\tau_{ij}\varepsilon_{ij}^s + \tau_{ni}u_{n,i}) \tag{18}$$

in which τ^s is residual stress and the residual surface stresses are expressed in Appendix B described as:

$$\tau_{11}^{s(B)} = \tau^{s(B)} + E^{s(B)}\varepsilon_{11}^s \tag{19}$$

$$\tau_{31}^{s(b)} = \frac{\partial w(x)}{\partial x} \tag{20}$$

$$\tau_{11}^{s(P)} = \tau^{s(P)} + E^{s(P)}\varepsilon_{11}^s - e_{31}^{s(P)}E_3 \tag{21}$$

$$\tau_{31}^{s(P)} = \frac{\partial w(x)}{\partial x} \tag{22}$$

$$\varepsilon_{11}^s = \varepsilon_{11} \tag{23}$$

The comprehensive measure of potential energy within the model can be explicated:

$$\Pi^{Total\ \ strain\ \ energy} = U^{Bulk} + U^{Actuator} + U^{Sensor} \tag{24}$$

Where strain energy included as surface layer and stress components using SGT $U^{Bulk} = U^{(B)} + U_s^{(B)}$, $U^{Actuator} = U^{(A)} + U_s^{(A)}$ and $U^{Sensor} = U^{(S)} + U_s^{(S)}$.

In addition, Kinetic energy of the system can be evaluated [62]:

$$T^{(B)} = \frac{1}{2}\int_0^L \left\{ I_0^{(B)}\left(\frac{\partial w}{\partial t}\right)^2 + I_2^{(B)}\left(\frac{\partial^2 w}{\partial x \partial t}\right)^2 \right\} dx \tag{25}$$

$$T^{(P)} = \frac{1}{2}\int_0^L \left\{ I_0^{(P)}\left(\frac{\partial w}{\partial t}\right)^2 + I_2^{(p)}\left(\frac{\partial^2 w}{\partial x \partial t}\right)^2 \right\} dx$$

in which,

$$I_0^{(B)} = \int_{A^{(B)}} \rho_B dA^{(B)}, \quad I_2^{(B)} = \int_{A^{(B)}} \rho_B Z^2 dA^{(B)} \tag{26}$$

$$I_0^P = \int_{A^{(P)}} \rho_P dA^{(P)}, \quad I_2^{(P)} = \int_{A^{(P)}} \rho_P Z^2 dA^{(P)}$$

ρ_B and ρ_P are the densities of the model. The total Kinetic energy can be simplified as:

$$\Pi^{Total\ \ strain\ \ energy} = T^{Bulk} + T^{Actuator} + T^{Sensor} \tag{27}$$

Where Kinetic energy included as surface layer and stress components based on SGT $T^{Bulk} = T^{(B)} + T_s^{(B)}$, $T^{Actuator} = T^{(A)} + T_s^{(A)}$ and $T^{Sensor} = T^{(S)} + T_s^{(S)}$.

By utilizing Hamilton's principle and the variation method, it is possible to derive the governing equations of motion.:

$$\delta \int_{t_1}^{t_2} \left(\Pi^{Total\ \ strain\ \ energy} - \Pi^{Total\ \ kinetic\ \ energy} \right) dt = 0 \tag{28}$$

The final equations of motion can be obtained by arranging the variables yields as follows [60]:

$$\begin{aligned}
\delta w : {} & \frac{1}{2}bE^b\left[\frac{h_0^3}{12}\right] + \frac{1}{2}C_{11}^{(a)}b\left[\frac{\left(\frac{h_0}{2}+h^{(a)}\right)^3}{3} - \frac{\left(\frac{h_0}{2}\right)^3}{3}\right] \\
& + \frac{1}{2}C_{11}^{(s)}b\left[\frac{\left(-\frac{h_0}{2}\right)^3}{3} - \frac{\left(-\frac{h_0}{2}-h^{(s)}\right)^3}{3}\right] + \mu^{(s)}l_2^2A^{(s)} + \mu^{(a)}l_2^2A^{(a)} \\
& + \mu^{(b)}l_2^2A^{(b)} + 2\mu^{(b)}l_0^2A^{(b)} \\
& + 2\mu^{(a)}l_0^2A^{(a)} + 2\mu^{(s)}l_0^2A^{(s)} + \frac{8}{15}\mu^{(b)}l_1^2A^{(b)} + \frac{8}{15}\mu^{(a)}l_1^2A^{(a)} + \frac{8}{15}\mu^{(s)}l_1^2A^{(s)} \\
& + E^{s(a)}\frac{h^2}{4}b + 2\left(-\frac{h_0^3}{24} + \frac{h^3}{24}\right)E^{s(a)} + E^{s(a)}\frac{h_0^2}{4}b + E^{s(b)}b\frac{h_0^2}{2} \\
& + E^{s(b)}\frac{h_0^3}{6} + E^{s(s)}\frac{h^2}{4}b + 2\left(-\frac{h^3}{24} + \frac{h_0^3}{24}\right)E^{s(s)} + E^{s(s)}\frac{h_0^2}{4}b\left(\frac{\partial^4 w}{\partial x^4}\right) \\
& \left(-2\mu^{(a)}l_0^2I^{(a)} - 2\mu^{(s)}l_0^2I^{(s)} - 2\mu^{(b)}l_0^2I^{(b)} - \frac{4}{5}\mu^{(b)}l_1^2I^{(b)} - \frac{4}{5}\mu^{(a)}l_1^2I^{(a)}\right. \\
& \left. - \frac{4}{5}\mu^{(s)}l_1^2I^{(s)}\right)\left(\frac{\partial^6 w}{\partial x^6}\right) + \left(\frac{1}{2}e_{31}b\left[\frac{1}{\beta}\left(\left(\cos\left(\beta\left(\frac{h_0}{2}+h^{(a)}\right)\right)\right.\right.\right.\right. \\
& \left.\left.\left.\left. - \cos\left(\beta\frac{h_0}{2}\right)\right)\right) + \left(\frac{h_0}{2}+h^{(a)}\right)\left(\sin\left(\beta\left(\frac{h_0}{2}+h^{(a)}\right)\right)\right)\right) \\
& - \left(\frac{h_0}{2}\right)\sin\left(\beta\frac{h_0}{2}\right)\Bigg] + \frac{1}{2}e_{31}^{s(a)}b\beta\left(-\frac{h}{2}\right)\cos\left(-\frac{h}{2}\beta\right) \\
& + e_{31}^{s(a)}\left[\frac{1}{\beta}\cos\left(-\frac{h_0}{2}\beta\right) - \frac{h_0}{2}\sin\left(-\beta\frac{h_0}{2}\right) - \frac{1}{\beta}\cos\left(-\frac{h}{2}\beta\right)\right. \\
& \left. + \frac{h}{2}\sin\left(-\beta\frac{h}{2}\right)\right] + \frac{1}{2}e_{31}^{s(a)}(b)\left(-\frac{h_0}{2}\right)\beta\cos\left(-\frac{h_0}{2}\beta\right)\Bigg)\left(\frac{\partial^2\phi^{(a)}}{\partial x^2}\right) \\
& + \left(\frac{1}{2}e_{31}b\left[\frac{1}{\beta}\left(\cos\left(-\beta\frac{h_0}{2}\right) - \cos\left(\beta\left(-\frac{h_0}{2}-h^{(s)}\right)\right)\right)\right.\right. \\
& \left.\left. - \left(\frac{h_0}{2}\right)\sin\left(-\beta\frac{h_0}{2}\right) + \left(\frac{h_0}{2}+h^{(s)}\right)\left(\sin\left(\beta\left(-\frac{h_0}{2}-h^{(s)}\right)\right)\right)\right)\right] \\
& + \frac{1}{2}e_{31}^{s(s)}b\beta\left(\frac{h}{2}\right)\cos\left(\frac{h}{2}\beta\right) \\
& + e_{31}^{s(s)}\left[\frac{1}{\beta}\cos\left(\frac{h}{2}\beta\right) + \frac{h}{2}\sin\left(\beta\frac{h}{2}\right)\right. \\
& \left. - \frac{1}{\beta}\cos\left(\frac{h_0}{2}\beta\right) - \frac{h_0}{2}\sin\left(\beta\frac{h_0}{2}\right)\right] + \frac{1}{2}e_{31}^{s(s)}b\left(\frac{h_0}{2}\right)\beta\cos\left(\frac{h_0}{2}\beta\right)\Bigg)\left(\frac{\partial^2\phi^{(S)}}{\partial x^2}\right) \\
& + \left(-\rho^{(a)}I^{(a)} - \rho^{(S)}I^{(S)} - \rho^{(b)}I^{(b)}\right)\left(\frac{\partial^4 w}{\partial x^2 \partial t^2}\right) \\
& + \left(\rho^{(a)}A^{(a)} + \rho^{(s)}A^{(s)} + \rho^{(b)}A^{(b)}\right)\left(\frac{\partial^2 w}{\partial t^2}\right) = 0
\end{aligned} \tag{29}$$

$$\begin{aligned}
\delta\phi^{(a)} : {} & \left(\frac{1}{2}e_{31}bh^{(a)} + e_{31}^{s(a)}\left[\frac{1}{\beta}\cos\left(-\frac{h_0}{2}\beta\right) - \frac{h_0}{2}\sin\left(-\beta\frac{h_0}{2}\right)\right.\right. \\
& \left. - \frac{1}{\beta}\cos\left(-\frac{h}{2}\beta\right) + \frac{h}{2}\sin\left(-\beta\frac{h}{2}\right)\right] + \frac{1}{2}e_{31}^{s(a)}(b)\left(-\frac{h_0}{2}\right)\beta\cos\left(-\frac{h_0}{2}\beta\right) \\
& + \frac{1}{2}e_{31}^{s(a)}b\beta\left(-\frac{h}{2}\right)\cos(-\frac{h}{2}\beta)\Bigg)\left(\frac{\partial^2 w}{\partial x^2}\right) - \frac{1}{2}\epsilon_{33}\beta b\left[\cos\left(\beta\left(\frac{h_0}{2}+h^{(a)}\right)\right)\right. \\
& \left. - \cos\left(\beta\frac{h_0}{2}\right)\right](\phi^{(a)}) = 0
\end{aligned}$$

$$\begin{aligned}
\delta\phi^{(s)} : {} & \left(\frac{1}{2}e_{31}bh^{(s)} + \frac{1}{2}e_{31}^{s(s)}b\left(\frac{h_0}{2}\right)\beta\cos\left(\frac{h_0}{2}\beta\right) + \frac{1}{2}e_{31}^{s(s)}b\beta\left(\frac{h}{2}\right)\cos\left(\frac{h}{2}\beta\right)\right. \\
& + e_{31}^{s(s)}\left[\frac{1}{\beta}\cos\left(\frac{h}{2}\beta\right) + \frac{h}{2}\sin\left(\beta\frac{h}{2}\right) - \frac{1}{\beta}\cos\left(\frac{h_0}{2}\beta\right) - \frac{h_0}{2}\sin\left(\beta\frac{h_0}{2}\right)\right]\left(\frac{\partial^2 w}{\partial x^2}\right)\Bigg) \\
& - \frac{1}{2}\epsilon_{33}\beta b\left[\cos\left(-\beta\frac{h_0}{2}\right) - \cos\left(\beta\left(-\frac{h_0}{2}-h^{(S)}\right)\right)\right](\phi^{(s)}) = 0
\end{aligned}$$

3. Solution Methodology

This section explores procedure to vibration and control of micro sandwich multilayer beam model based on SGT and surface theory. The boundary cantilever micro-beam conditions of the structure and higher order are expressed as [20,63]:

$$w(0) = 0 \tag{30}$$

$$\frac{\partial w(0)}{\partial x} = 0$$

$$\frac{\partial^2 w(L)}{\partial x^2} = 0$$

$$\frac{\partial^3 w(L)}{\partial x^3} = 0$$

$$\left(\mu^{(b)}+\mu^{(a)}+\mu^{(s)}\right)\left(I^{(b)}+I^{(a)}+I^{(s)}\right)\left(2l_0^2+\frac{4}{5}l_1^2\right)\frac{\partial^3 w(0)}{\partial x^3}$$
$$= \left(\mu^{(b)}+\mu^{(a)}+\mu^{(s)}\right)\left(I^{(b)}+I^{(a)}+I^{(s)}\right)\left(2l_0^2+\frac{4}{5}l_1^2\right)\frac{\partial^3 w(L)}{\partial x^3} = 0 \tag{31}$$

$$-\begin{pmatrix}\left(E^{(b)}+E^{(a)}+E^{(s)}\right)\left(I^{(b)}+I^{(a)}+I^{(s)}\right)+\left(\mu^{(b)}+\mu^{(a)}+\mu^{(s)}\right)\left(A^{(b)}\\ +A^{(a)}+A^{(s)}\right)\\ \left(2l_0^2\right.\\ \left.+\frac{8}{15}l_1^2+l_2^2\right)\end{pmatrix}$$

$$\frac{\partial^3 w(L)}{\partial x^3}+\left(\mu^{(b)}+\mu^{(a)}+\mu^{(s)}\right)\left(I^{(b)}+I^{(a)}+I^{(s)}\right)\left(2l_0^2+\frac{4}{5}l_1^2\right)\frac{\partial^5 w(L)}{\partial x^5} = 0$$

$$\begin{pmatrix}\left(E^{(b)}+E^{(a)}+E^{(s)}\right)\left(I^{(b)}+I^{(a)}+I^{(s)}\right)\\ +\left(\mu^{(b)}+\mu^{(a)}+\mu^{(s)}\right)\left(A^{(b)}+A^{(a)}+A^{(s)}\right)\\ \left(2l_0^2+\frac{8}{15}l_1^2+l_2^2\right)\end{pmatrix}$$

$$\frac{\partial^2 w(L)}{\partial x^2}-\left(\mu^{(b)}+\mu^{(a)}+\mu^{(s)}\right)\left(I^{(b)}+I^{(a)}+I^{(s)}\right)\left(2l_0^2+\frac{4}{5}l_1^2\right)\frac{\partial^4 w(L)}{\partial x^4} = 0$$

This study uses DQM to study the control and dynamic behavior of structures. In this numerical solution, the corresponding differential equation of construction is transformed into a series of linear algebraic equations using weighting factors [3,64–66]. The weighted linear sum of the function values in this coordinate direction is used as the grid points' derivative of the function. The development of the partial derivatives of a function and the Lagrange interpolation basis functions can be achieved [67,68]:

$$f^{(r)}(x_i) = \sum_{i=1}^{N} C_{ij}^{(n)} f(x_i), i = 1, 2, \ldots, N \tag{32}$$

$$C_{ij}^{(1)} = \begin{cases} \prod_{k=1,k\neq i}^{N}(x_i - x_k) \Big/ \prod_{k=1,k\neq i}^{N}(x_j - x_k) & (i \neq j) \\ \sum_{k=1,k\neq i}^{N} \frac{1}{(x_i - x_k)} & (i = j) \end{cases} \tag{33}$$

$$A_{ij}^{(2)} = \sum_{K=1}^{N} A_{ik}^{(1)} A_{kj}^{(1)}$$

$$A_{ij}^{(3)} = \sum_{K=1}^{N} A_{ik}^{(1)} A_{kj}^{(2)} = \sum_{K=1}^{N} A_{ik}^{(2)} A_{kj}^{(1)}$$

$$A_{ij}^{(4)} = \sum_{K=1}^{N} A_{ik}^{(1)} A_{kj}^{(3)} = \sum_{K=1}^{N} A_{ik}^{(3)} A_{kj}^{(1)}$$

$$A_{ij}^{(5)} = \sum_{K=1}^{N} A_{ik}^{(1)} A_{kj}^{(4)} = \sum_{K=1}^{N} A_{ik}^{(4)} A_{kj}^{(1)}$$

$$A_{ij}^{(6)} = \sum_{K=1}^{N} A_{ik}^{(1)} A_{kj}^{(5)} = \sum_{K=1}^{N} A_{ik}^{(5)} A_{kj}^{(1)}$$

where $C_{ij}^{(n)}$, (N) and (r) indicate the weighting coefficients, number of grid points and the order of derivation, respectively. The selection of grid points and weighting coefficients played a pivotal role in ensuring the precision of the outcomes [69,70]. The grid factors are taken into consideration through Chebyshev–Gauss–Lobatto relation as [71,72]:

$$x_i = \frac{1}{2}\left[1 - \cos\left(\frac{(i-1)\pi}{N-1}\right)\right]$$

$$i = 1, 2, \ldots N \tag{34}$$

The discretized equations can be expressed as:

$$\delta w : \left(A_1 + A_2 + A_3 + A_{12} + A_{13} + A_{14} + A_{15} + A_{16} + A_{17}\right.$$
$$\left. + A_{18} + A_{19} + A_{20} + B_1^S + B_4^S + B_6^S + B_8^S + B_{10}^S + B_{14}^S + B_{15}^S\right) \sum_{1}^{N} A_{ik}^{(4)} w_k$$

$$+ \left(A_{21} + A_{22} + A_{23} + A_{24} + A_{25} + A_{26}\right) \sum_{1}^{N} A_{ik}^{(6)} w_k$$

$$+ \left(A_4 + B_2^S + B_5^S + B_7^S\right) \sum_{1}^{N} A_{ik}^{(2)} \phi_k^{(a)}$$

$$+ \left(A_5 + B_{11}^S + B_{13}^S + B_{16}^S\right) \sum_{1}^{N} A_{ik}^{(2)} \phi_k^{(s)}$$

$$+ \left(A_6\right) \sum_{1}^{N} A_{ik}^{(2)} w_k \left(\frac{\partial^2 w}{\partial t^2}\right) + \left(A_7\right)\left(\frac{\partial^2 w}{\partial t^2}\right) = 0$$

$$\delta\phi^{(a)} : \left(A_8 + B_5^S + B_7^S + B_2^S\right) \sum_{1}^{N} A_{ik}^{(2)} w_k + \left(A_9\right)\left(\phi^{(a)}\right) = 0$$

$$\delta\phi^{(s)} = \left(A_{10} + B_{16}^S + B_{11}^S + B_{13}^S\right) \sum_{1}^{N} A_{ik}^{(2)} w_k + \left(A_{11}\right)\left(\phi^{(s)}\right) = 0 \tag{35}$$

The coefficient of the above-discretized equations is explained in Appendix C.

The discretized Eq. (35) and the related boundary conditions can be presented into matrices using stiffness matrices $[K]$ and mass matrices $[M]$ and Rayleigh damping matrix $[C]$, respectively [18,73–75]:

$$\left([M]\left\{\ddot{X}\right\} + [C]\left\{\dot{X}\right\} + [K]\{X\}\right) = \{F\}$$

$$[C] = \alpha_1 \quad [M] + \alpha_2 \quad [K]$$

$$\left(\begin{bmatrix} M^{ww} & 0 & 0 \\ 0 & 0 & 0 \\ 0 & 0 & 0 \end{bmatrix} \begin{Bmatrix} \ddot{W} \\ \ddot{\Phi}_{(a)} \\ \ddot{\Phi}_{(s)} \end{Bmatrix} + \begin{bmatrix} C^{ww} & C^{w\Phi_{(a)}} & C^{w\Phi_{(s)}} \\ C^{\Phi_{(a)}w} & C^{\Phi_{(a)}\Phi_{(a)}} & C^{\Phi_{(a)}\Phi_{(s)}} \\ C^{\Phi_{(s)}w} & C^{\Phi_{(s)}\Phi_{(a)}} & C^{\Phi_{(s)}\Phi_{(s)}} \end{bmatrix} \begin{Bmatrix} \dot{W} \\ \dot{\Phi}_{(a)} \\ \dot{\Phi}_{(s)} \end{Bmatrix} + \begin{bmatrix} K^{ww} & K^{w\Phi_{(a)}} & K^{w\Phi_{(s)}} \\ K^{\Phi_{(a)}w} & K^{\Phi_{(a)}\Phi_{(a)}} & 0 \\ K^{\Phi_{(s)}w} & 0 & K^{\Phi_{(s)}\Phi_{(s)}} \end{bmatrix} \begin{Bmatrix} W \\ \Phi_{(a)} \\ \Phi_{(s)} \end{Bmatrix} \right) = \begin{Bmatrix} P \\ F_{(a)} \\ 0 \end{Bmatrix} \tag{36}$$

The relevant equations for a cantilever sandwich micro piezoelectric beam by using strain gradient theory and surface energy are expressed in a compact matrix, where α_1, α_2 and $[K^{ww}]$, $[K^{w\Phi}]\left(=[K^{w\Phi}]^T\right)$ and $[K^{\Phi\Phi}]$ are Rayleigh coefficients and mechanical stiffness matrix, electrical mechanical coupling stiffness matrix and piezoelectric permittivity matrix respectively [50,76,77].

$$[M^{ww}]\left\{\ddot{W}\right\} + \left[[K^{ww}] - [K^{w\Phi_{(s)}}][K^{\Phi_{(s)}\Phi_{(s)}}]^{-1}[K^{\Phi_{(s)}w}]\right]\{W\} = \{P\} - [K^{w\Phi_{(a)}}]\left\{\Phi_{(a)}\right\} \tag{37}$$

$$\left\{\Phi_{(s)}\right\} = [-K^{\Phi_{(s)}\Phi_{(s)}}]^{-1}[K^{\Phi_{(s)}w}]\{w\}$$

In this study design of LQR and LQI controller with the help of MATLAB software have been completed. With assuming full state feedback as Eq. (38), the control law is stated by [48,78–80]:

$$\{\dot{z}\} = [A]\{z\} + [B]\left\{\Phi_{(a)}\right\} \tag{38}$$

$$[y] = [C_0]\{z\}$$

$$X = [z \quad \dot{z}]^T$$

$$[A] = \begin{bmatrix} [I] & [0] \\ -[M]^{-1}[C] & -[M]^{-1}[K] \end{bmatrix}$$

$$[B] = \begin{bmatrix} 0 \\ -[M]^{-1}[\psi]^T[K^{w\Phi_{(a)}}] \end{bmatrix}$$

$$[\widehat{B}] = \begin{bmatrix} [0] \\ [\psi]^T\{F\} \end{bmatrix}$$

$[A]$, $[B]$ and $[\widehat{B}]$ are the system, control and disturbance matrices and $[C_0]$ is output matrix, respectively. To control the deflection behavior and vibration oscillation of the system, a linear quadratic regulator (LQR) optimal control and linear quadratic integral (LQI) controller are utilized [81,82]. Feedback control systems are outlined to acquire indicated necessities for transient response, steadiness limits, or pole positions in a closed control circle. The criterion function of LQR control is [8,83]:

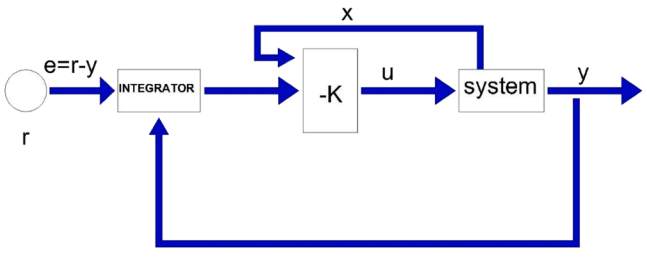

Fig. 1. The LQI control scheme.

$$J = \int_0^\infty \left(\{y\}^T[Q]\{y\} + \{V_a\}^T[R]\{V_a\}\right)dt \tag{39}$$

$$\{V_a\} = -[G_c]\{z\} = -[R]^{-1}[B]^T[\widehat{P}]\{z\} \tag{40}$$

where $[Q]$ and $[R]$ are a symmetric matrix for the control performance and control cost. The $R = rI$ and $[Q]$ is presented as:

$$Q = q\begin{bmatrix} [\psi]^T[K][\psi] & 0 \\ 0 & [\psi]^T[M][\psi] \end{bmatrix} \tag{41}$$

where $[G_c]$ is the control gain matrix and $[\widehat{P}]$ is the positive definite Riccati matrix of the truncated system[5]. It good to mention that the LQR controller aims to minimize a cost function that represents the trade-off between control effort and system performance[34]. The Riccati matrix defined as:

$$[A]^T[\widehat{P}] + [\widehat{P}][A]^T - [\widehat{P}][B][R]^{-1}[\widehat{P}] + [\overline{C}_0]^T[Q][\overline{C}_0] = 0 \tag{42}$$

The Riccati equation provides a connection between the state and input matrices of the system and the optimal control law. Once the Riccati matrix P is computed, the optimal control law can be derived by solving for the control input u as:

LQI control systems are widely used such as dynamic positioning of floating maritime platforms, electromechanical suspension control, depth and course control of unmanned underwater vehicles, attitude / position control of unmanned aerial vehicles [84]. The LQI scheme is given in Fig. 1.

Plant applied to step state and output disturbances for LQI is considered as [85]:

$$\dot{z} = A_s(t) + B_s(t)V_{fb}^*$$

$$y_s^* = C_sZ + D_sV_{fb}^* \tag{43}$$

Where $y_s^* = \sum_s^{-1}U_s^TQ^{1/2}y$, $A_s(t) = A(t)$, $B_s(t) = B(t)R^{-1/2}V_s$, $C_s = \sum_s^{-1}U_s^TQ^{1/2}$ and $D_s = 0$.

Define the integration of tracking errors under the step reference [52,86,87].

$$e(t) = \int_0^t (r - y(t))dt \tag{44}$$

$$\dot{e}(t) = r - d_y - Cx(t)$$

Table 1
Materials and geometric properties of SGT microbeams integrated with piezoelectric layers.

Parameters		Bulk	Piezoelectric layer
Thickness	H (μm)	3	3
Length	L (μm)	450	450
Width	b (μm)	50	50
Young's modulus	E (GPa)	210	64
Mass density	$\rho(kg/m^3)$	2331	7500
Poisson's ratio	υ	0.24	0.27
piezoelectric coefficients	$e_{31}(C/m^2)$	-	-10
Dielectric permittivity constant	$\in_{33}$ (C^2/m^2N)	-	1.0275×10^{-8}
Higher order parameters	$l(\mu m)$	17.6	17.6
Surface piezoelectric coefficients	$e_{31}^s(C/m^2)$	-	-3×10^{-8}
Lame coefficients of surface layer	$\lambda_s(C/m^2)$	4.488	-4.488
Lame coefficients of surface layer	$\mu_s(C/m^2)$	2.774	-2.774
residual stress	$\tau^s(N/m)$	0.605	0.605
Density of surface layer	$\rho_s(kg/m^2)$	3.17×10^{-7}	3.17×10^{-7}

With considering the above equations as a result, the system is expanded [85].

$$\begin{bmatrix} \dot{x}(t) \\ \dot{e}(t) \end{bmatrix} = \begin{bmatrix} A_s & 0 \\ -C_s & 0 \end{bmatrix} \begin{bmatrix} x(t) \\ e(t) \end{bmatrix} + \begin{bmatrix} B_s \\ 0 \end{bmatrix} u(t) + \begin{bmatrix} d_x \\ r - d_y \end{bmatrix} \tag{45}$$

To solve the LQI design problem, we define an extended state vector containing the integral of the meaningful output over time y_s^*

$$x = \begin{bmatrix} \int_0^t y_s^* dt' \\ z \end{bmatrix}$$

$$\min J_+ = \frac{1}{2} \int_{t_0}^{\infty} \left[x^t Q x + \left(V_{fb}^* \right)^T + V_{fb}^* \right] \mathrm{dt} \tag{46}$$

4. Results and discussion

In this section, the impact of controller simulation on SGT micro-beam, in conjunction with a piezoelectric layer, is presented. The vibrational behavior and suppression of SGT microbeams, which are embedded in piezoelectric layers, are analyzed using LQR and LQI controllers. For this task, the controller was numerically tested and tracked using a MATLAB software application. The material and geometrical properties are given in Table 1 [47,50].

4.1. Validation

Before investigation the controller design simulation for micro sandwich beam model based on higher order theory, the equation of motion should be verified; therefore, this section compares the results obtained with other work by Kong. et al. [88] considering some qualifications. In addition, the results of MCST model are presented in a previous study by the Khaje Khabaz et al. [50]. In Fig. 2, comparison of the vibrational behavior of present simulation is displayed. Based on the comparison with the analytical solution presented in reference [88] a remarkable level of concurrence has been achieved between the current findings and the aforementioned analytical results. This figure depicts the accuracy of the GDQM for the first two vibrational modes of the cantilever micro-beam integrated with piezoelectric layers, according to the classical continuum theory. It is discernible that the precision of the vibrational modes intensifies with an increase in the number of grid points. Furthermore, the vibration mode shapes of the model are demonstrated to be in favorable agreement with the associated boundary conditions. This result is consistent with previous observation, where the higher order theories were found to elevate the natural frequency. Incorporation of these theories lead to an augmented assessment of the system's stiffness.

Table 2
Comparison of RMS based on different theories.

SGT	MCST	CT	Parameters	Initial condition
1.0106e-5	1.0113e-5	1.1490e-5	RMS	0.05 ×L
2.423e-5	2.446e-5	2.757e-5	RMS	0.12 ×L

4.2. LQR controller design

Table 2 presents a comparative analysis of the numerical dynamic response outcomes of the root mean square amplitude (RMS) of a micro beam integrated with piezoelectric layers utilizing different higher order theories. The comparative results were obtained by implementing initial tip displacements of magnitudes 5% and 12% of the beam length. The results compared with previous study presented by Khaje Khabaz et al. [50] and as it clear by employing the SGT, leads to reduction, in the maximum amplitude deflections parameter of the microbeam with comparing by other theories. The aforementioned outcome can be substantiated by the augmentation of the micro-beam stiffness matrix in the SGT model.

To evaluate the efficiency of the proposed LQR controller, various weighting matrices R are used. Fig. 3 shows the effect of various velocity feedback gains on the tip deflection of SGT micro sandwich beam model. The results are obtained by subjecting 1 N impulse at the tip of the model and then the controller tuned. It can be found that with the aid of using growing weighting matrix R, the end deflection of the reaction system is decreased. It can be obtained that with considering the lower weighting R matric, the dynamic deflection of generation of an active damp structure is higher. From this data, one may deduce that an increase in micro-beam length results in a decrease in natural frequency sensitivity.

Fig. 4 illustrates the impact of utilizing the optimal control voltage on the stabilization duration of the SGT micro sandwich beam model. Using feedback gain results in transient suppression and model amplitude suppression. As illustrated, with increasing the weighting matrix R the settling time of model and control voltage of actuator will be decreased. Comparison results of present study and the last study given by Khaje khabaz et al. [50] show that maximum control voltage related to SGT model has higher magnitude. Also, better call for control enters voltage and the voltage control cause lowering the dynamic reaction

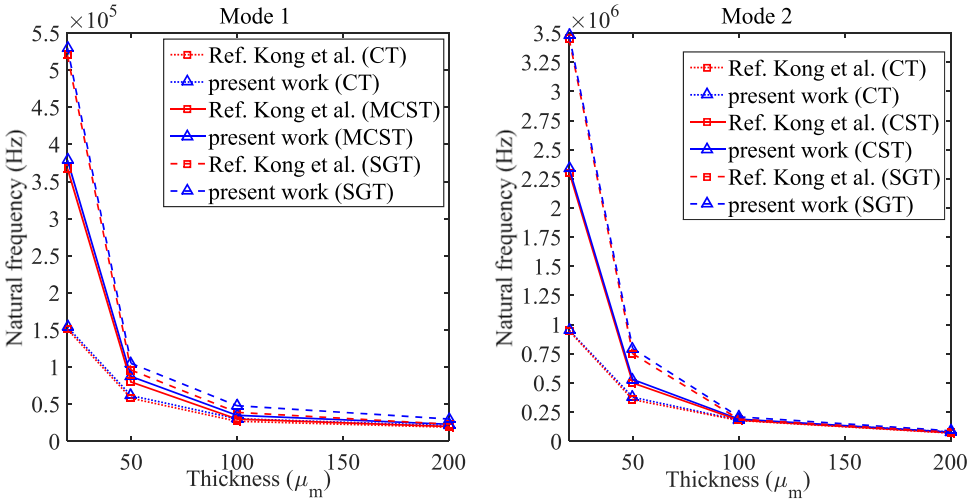

Fig. 2. Comparison of the vibrational behavior of present simulation and Kong et al. [88].

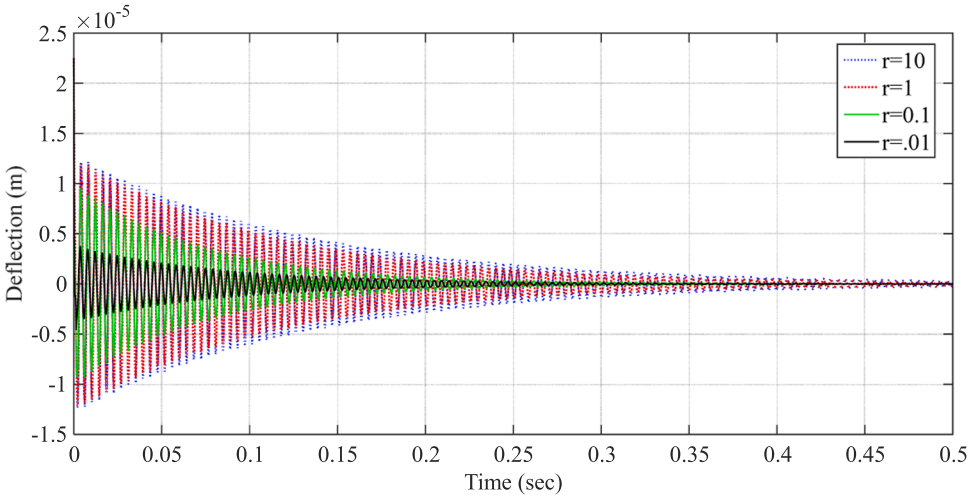

Fig. 3. Effect of various velocity feedback gains on tip deflection of the SGT micro sandwich beam model.

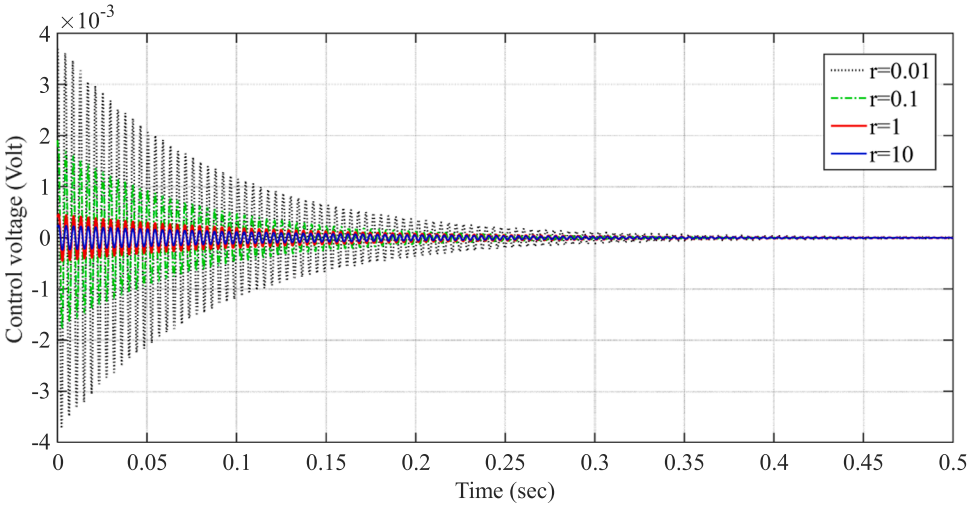

Fig. 4. Maximum actuator voltage r parameter variation of the of SGT micro sandwich model.

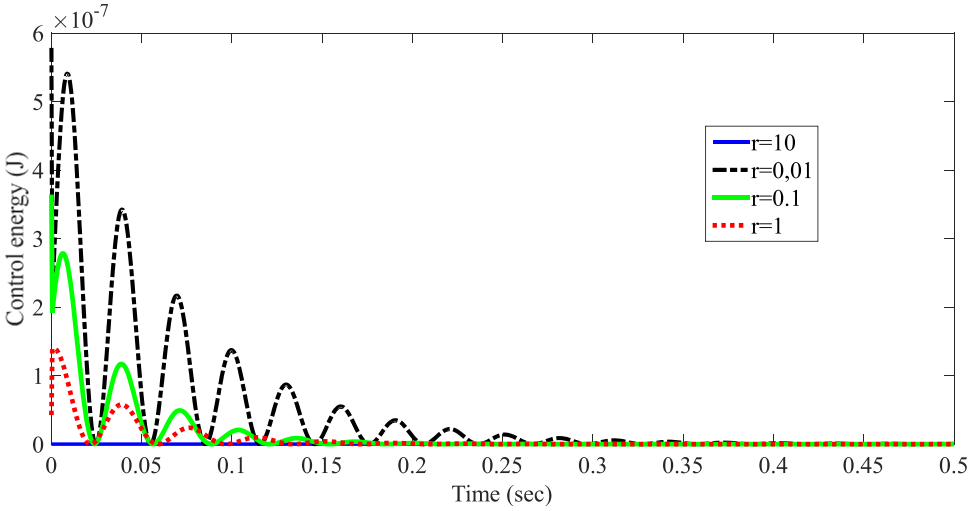

Fig. 5. Effect of various r parameter on energy control time response of the SGT micro sandwich model.

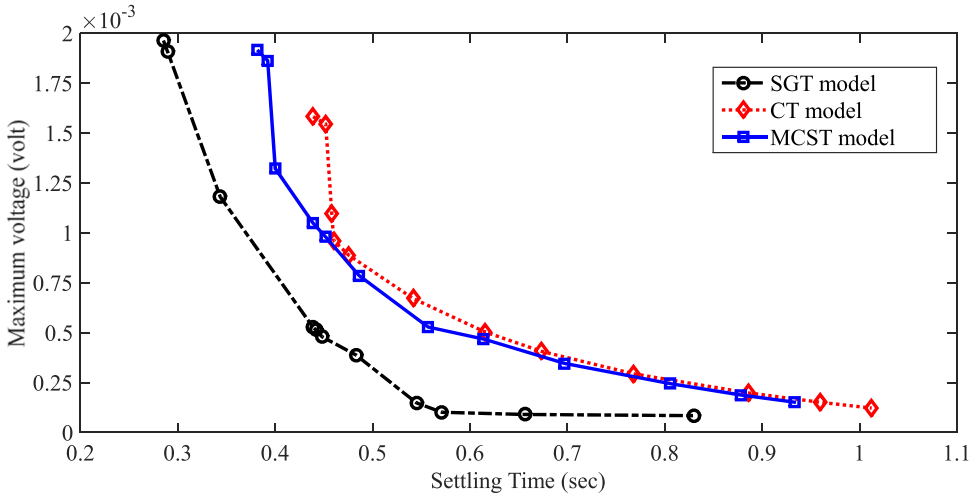

Fig. 6. Effect of CT, MCST and SGT theories on the variation of maximum voltage versus stabilization time.

velocities. To achieve rapid attenuation of vibration within a limited time frame, it is advisable to reduce the weighting matrices R. Conversely, increasing the weighting matrix R will result in a heightened feedback voltage signal on account of the peak value of the model displacement.

Fig. 5 displays the time–history responses of the energy control voltages in various conditions of r parameter of LQR actuator. From this figure, can be found that decreasing the r values of actuator can improve the vibration control effect apparently and increase the control voltage of system. However, due to the energy limitation and the structural condition, the energy of actuator cannot be increased infinitely. The results lead to the conclusion that the material length scale parameters hold considerable impact on the dynamic frequency and response of the model in small scale. This occurrence can be attributed to the increase in stiffness matrix of strain gradient and surface effects, which leads to a growth in the model's bending rigidity. Consequently, the amplitudes shift towards lower magnitudes and a significant increase in frequency is observed, in comparison to the MCST and classical theories.

For the purpose of conducting a comparative analysis, this study investigates the impact of maximum voltage on the settling time with respect to the CT, MCST, and SGT excitation theories as depicted in Fig. 6. The maximum vibration damping associated with the SGT micro sandwich beam model is also presented in this figure. These observed phenomena can be rationalized by the higher stiffness of the SGT model in comparison to that of the MCST and CT models. In other words, an increase in the stiffness of the model corresponds to a heightened requirement for voltage, while simultaneously reducing the stabilization time. It ought to be noted that, by taking into account the structural damping coefficient, the maximum control voltage increases when utilizing the SGT. As is evident, the total stiffness of the model becomes larger than that of its classical model. Therefore, the augmentation of model stiffness should contribute to an enhanced frequency and greater stability. Moreover, the velocities of dynamic response and settling time are significantly reduced in the model based on MCST. This increase in the maximum control voltage is attributed to the augmentation of the stiffness matrix, which is due to the increase in the length scale parameter effect. Furthermore, it can be inferred that the effect of the length scale parameter is also amplified. It is noteworthy to mention that

Table 3
Various values of R, Q and I parameter of SGT micro sandwich beam model.

	R	Q	I
Sys.1	1	5×10^3	6
Sys. 2	1	1×10^3	6
Sys.3	0.1	10	6
Sys.4	5	10	6
Sys.5	10	10	6

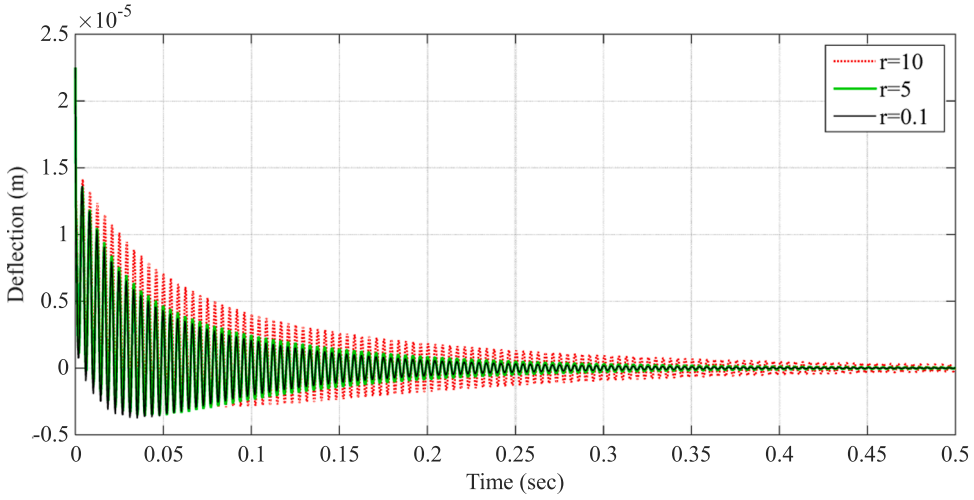

Fig. 7. Effect of the LQI tuning on the tip deflection of the SGT micro sandwich model.

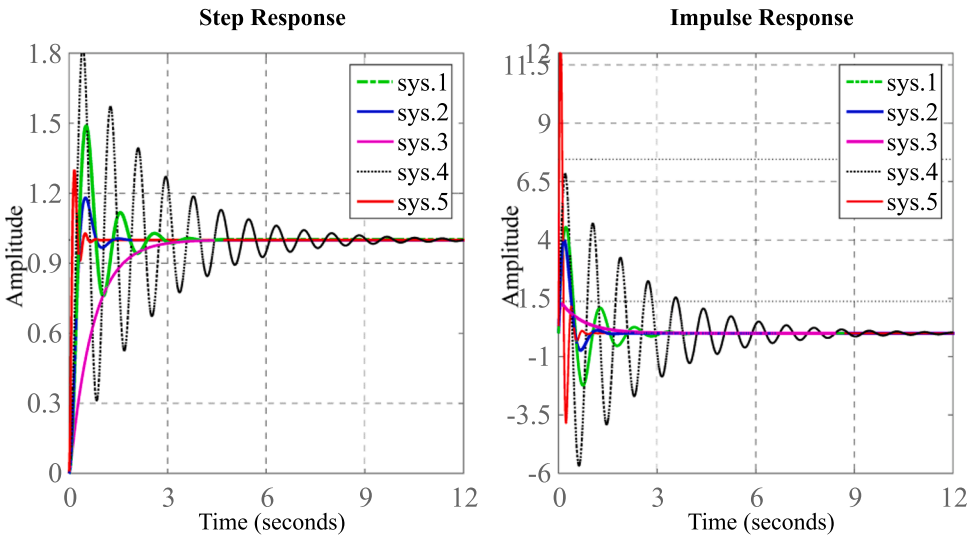

Fig. 8. Step and impulse respond for different LQI tuning.

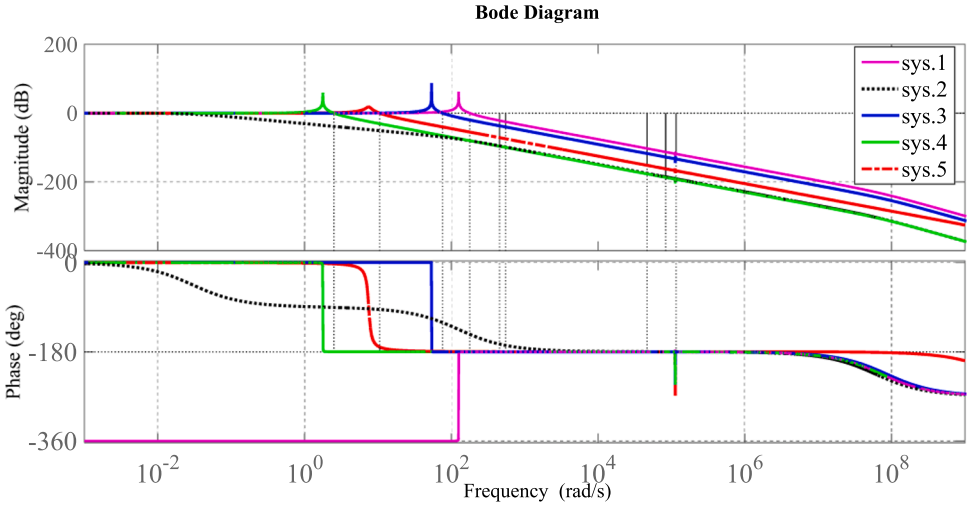

Fig. 9. The influence of different tuning of LQI controller on bode diagram of SGT micro sandwich beam model.

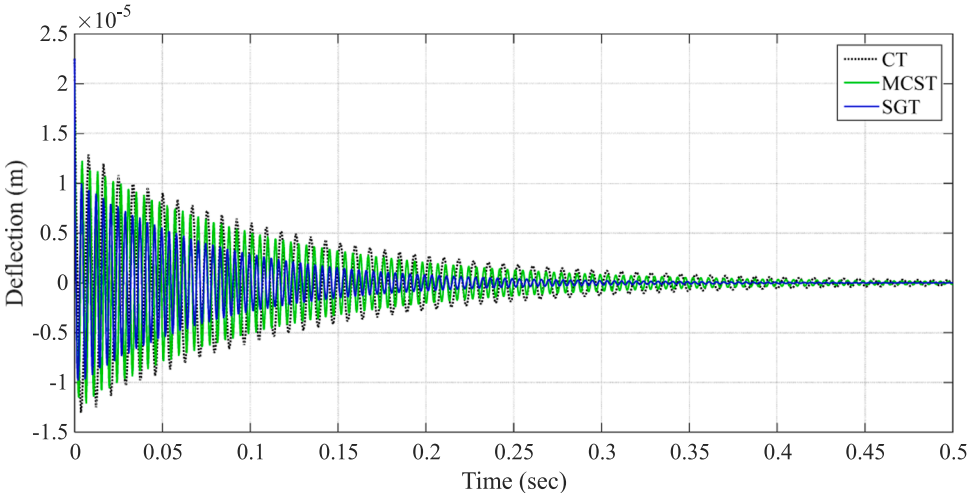

Fig. 10. LQR tuning time response of the micro sandwich beam model for CT, MCST and SGT theories.

the dynamic response of the system and the settling time are significantly reduced in the SGT model.

4.3. LQI controller Design

The present study demonstrates the variation of the control voltage in response to different weighting matrices R for a micro-beam equipped with piezoelectric actuator and sensor layers, situated on the top and bottom surfaces, respectively. This behavior is analyzed using the SGT under transient excitation. Controlled responses of the LQI tuning on the tip deflection of the SGT micro sandwich model shown in Fig. 7. As it can be concluded, the LQI tuning has a significant effect on the dynamic response of the micro-beam. In this case, LQI indicates a bit higher settling time in evaluation to LQR. It can be visible that with a lower in r ratio of the controller, the shape turns softer and the dynamic deflection of the device increases. In addition, with tuning the LQI to middle thickness ratio of the sandwich shape, the dynamic amplitude may be decreased. Additionally, it is observed that the input voltage is a function of the piezoelectric actuator layer. Our investigation shows that the LQI control approach is an effective method for controlling the vibration, as the optimal gain is obtained by minimizing the cost function.

Table 3 was used to evaluate the effect of the R, Q, and I parameter values on the SGT micro sandwich model. Fig. 8 shows the results of various adjustments to the LQI for the step and pulse diagrams of different cases of sandwich micro beam model. It is evident that an increase in the cost and quality factor matrixes leads to an elevation in the natural frequencies of the structure. This phenomenon can be attributed to the enhancement of mechanical properties of the piezoelectric material through the incorporation of microbeam, consequently augmenting the stiffness of the structure. In addition, Fig. 9 shows the effect of various adjustments of the LQI controller on the Bode plot of the SGT micro sandwich beam model. As can be seen from the improved performance and cost matrix, the mechanical properties of the piezoelectric material are improved, the rigidity of the structure is increased, and the natural frequency of the structure is increased.

Fig. 10 illustrates the effect of the LQI controller on the dynamic deflection of a micro sandwich beam with a CT, MCST, SGT piezoelectric actuator and sensor layer. All the results presented consider the LQR controller parameters R= 1 and Q= 5×10^3. As can be seen, considering the controller, the dynamic deflection of the CT micro-beam model is higher than when size-dependent theories such as MCST and SGT are used. In other words, using SGT reduces the dynamic displacement of the micro- sandwich beam model by about 29%. This is due to the increase in the stiffness matrix of increasing the periodic scale parameters related to the higher order theory. In addition, the SGT model requires significant reductions in dynamic reaction speed and settling time.

The amplitude of the excitation deflection is changed in the LQI controller to obtain different oscillatory displacements at the model with negative amplitude. The corresponding processes and results of the vibration suppression of LQI controller model by using on higher-order elasticity and surface theories are presented in Fig. 11. It can be obtained as the length scale material weight of the SGT decreases to the model the maximum of dynamic amplitude factor occurs in lower values of the deflection. It also can be concluded that the comparing control voltage in present study which predicted by the strain gradient elastic beam theory, is more than those of MCST and CT model that given by Khaje khabaz et al. [50]. Therefore, the LQI controller can effectively suppress the vibration and minimize tracking errors and controller effort of micro sandwich model.

Furthermore, as the length ratio is augmented, it results in noteworthy attenuation in dynamic systems and vibration suppression. This decline is associated with the stiffness matrix of the model. The impact of material length scale parameters $l_2$can be attributed to SGT.The aforementioned figure demonstrates that when the strain gradient theory is taken into account, the stiffness of the model is enhanced and the amplitudes are displaced towards smaller magnitudes.

5. Conclusion

The current investigation was focused on the modeling and dynamic regulation of a multi-layer sandwich composite piezoelectric micro beam utilizing the higher-order elasticity theory and surface energy. In addition, present study demonstrates that the cantilever microbeam model has a stabilizing effect based on the comparison of results. Within this inquiry, the ensuing noteworthy observations were garnered from the research:

- From this work, we can conclude that the dynamic deflection of the micro-beam model in CT is higher than when using size-dependent theories such as MCST and SGT, taking the controller into account. In other words, using SGT reduces the dynamic deflection of the micro-beam integrated with the piezo layer by about 29%.
- Utilizing the LQR and LQI method, dynamic vibration control can be strikingly effective in vibration decrease. In addition, LQL can satisfactorily satisfy the tracking issue
- The dynamic deflection for LQI simulation is lower and faster than LQR model.
- The dynamic response speed and settling time of the SGT model are greatly reduced by increasing the stiffness matrix.

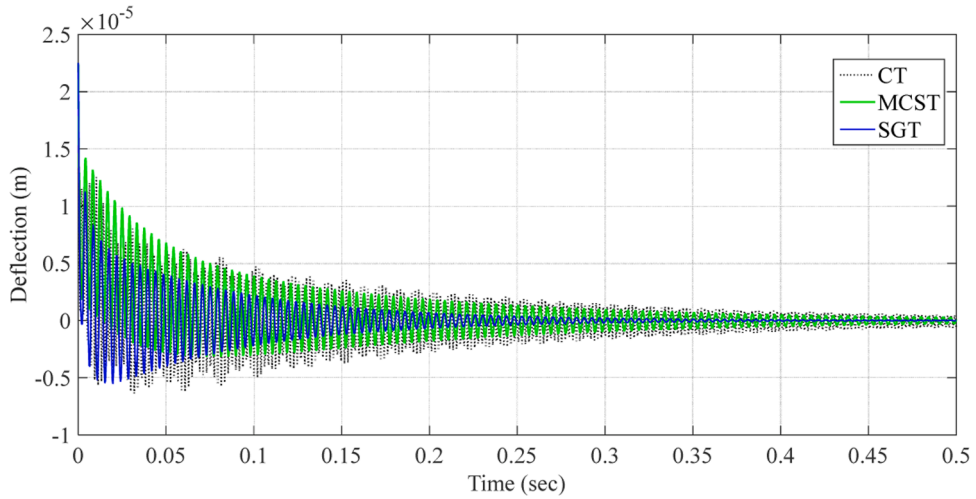

Fig. 11. LQI tuning time response of the micro sandwich beam model for CT, MCST and SGT theories.

- The comparing of control voltage shows that this parameters in sandwich sensor and actuator piezoelectric micro system based on strain gradient elastic beam theory, is more than those of model of MCST and CT.
- By considering SGT model the settling time of the system increase because the stiffness of model increase. Also, by increasing the stiffness, the settling time of the system decrease. Subsequently the maximum voltage increases in SGT, therefore the vibration of the structure is damped faster. It is important to note that the maximum control voltage increases when the structural damping coefficient is taken into consideration and the SGT is employed. This increase in the maximum control voltage can be attributed to the effect of the length scale parameter, which increases the stiffness matrix.
- Both the SGT and MCST incorporate material length scale parameters associated with symmetric rotation gradients subjected to classical stiffness. Consequently, the total stiffness of the model becomes larger than that of its classical counterpart, resulting in improved frequency and enhanced stability. Moreover, the model based on SGT exhibits significantly reduced dynamic response velocities and settling time.

Declaration of Competing Interest

The authors declare that they have no known competing financial interests or personal relationships that could have appeared to influence the work reported in this paper.

Appendix A

The relation of SGT can be defined as:

$$\sigma_{ij} = \lambda\delta_{ij}\varepsilon_{mm} + 2\mu\varepsilon_{ij} - e_{nij}E_n \tag{A-1}$$

$$\varepsilon_{ij} = \frac{1}{2}\left(u_{i,j} + u_{j,i}\right) \tag{A-2}$$

$$m_{ij} = 2\mu l_2^2\chi_{ij} \tag{A-3}$$

$$\chi_{ij} = \frac{1}{2}\left(\theta_{i,j} + \theta_{j,i}\right) \tag{A-4}$$

$$D_i = e_{imn}\varepsilon_{mm} + \epsilon_{im}E_m \tag{A-5}$$

$$E_i = -\Phi_{,i} \tag{A-6}$$

$$p_i = 2\mu l_0^2\gamma_i \tag{A-7}$$

$$\gamma_i = \varepsilon_{mm.i} \tag{A-8}$$

$$\eta_{ijk}^{(1)} = \frac{1}{3}\left(\varepsilon_{jk.i} + \varepsilon_{ki.j} + \varepsilon_{ij.k}\right) - \frac{1}{15}\delta_{ij}\left(\varepsilon_{mm.k} + 2\varepsilon_{mk.m}\right) - \frac{1}{15}\delta_{jk}\left(\varepsilon_{mm.i} + 2\varepsilon_{mi.m}\right) + \delta_{kj}\left(\varepsilon_{mm.j} + 2\varepsilon_{mj.m}\right) \tag{A-9}$$

$$\tau_{ijk}^{(1)} = 2\mu l_1^2\eta_{ijk} \tag{A-10}$$

$$\theta_i = \frac{1}{2}\left(curl\left(u_{i,j}\right)\right)_i \tag{A-11}$$

$$\lambda = \frac{E\upsilon}{(1+\upsilon)(1-2\upsilon)} \tag{A-12}$$

$$\mu = \frac{E}{2(1+\upsilon)} \tag{A-13}$$

Appendix B

The surface Gurtin–Murdoch continuum theory can be expressed [89] as:

$$\tau_{\alpha\beta} = \mu^s\left(u_{\alpha,\beta} + u_{\beta,\alpha}\right) + (\lambda^s + \tau^s)u_{k,k}\delta_{\alpha\beta} + \tau^s(\delta_{\alpha\beta} - u_{\beta,\alpha}) \tag{B-1}$$

$$\tau_{n\alpha} = \tau^s(u_{n,\alpha}) \tag{B-2}$$

Which $\tau^s$is residual stress, E^s is surface elastic and υ^S is surface Poisson's ratio. λ^s and μ^s are given by:

$$\lambda^s = \frac{E^s\upsilon^S}{(1+\upsilon^S)(1-2\upsilon^S)} \tag{B-3}$$

$$\mu^s = \frac{E^s}{2(1+\upsilon^S)} \tag{B-4}$$

Appendix C

$$A_1 = \frac{1}{2} b E^b \left[\frac{h_0^3}{12}\right]$$

$$A_2 = \frac{1}{2} C_{11}^{(a)} b \left[\frac{\left(\frac{h_0}{2} + h^{(a)}\right)^3}{3} - \frac{\left(\frac{h_0}{2}\right)^3}{3}\right]$$

$$A_3 = \frac{1}{2} C_{11}^{(s)} b \left[\frac{\left(-\frac{h_0}{2}\right)^3}{3} - \frac{\left(-\frac{h_0}{2} - h^{(s)}\right)^3}{3}\right]$$

$$A_4 = \frac{1}{2} e_{31} b \left[\frac{1}{\beta}\left(\left(\cos\left(\beta\left(\frac{h_0}{2} + h^{(a)}\right)\right) - \cos\left(\beta\frac{h_0}{2}\right)\right)\right) + \left(\frac{h_0}{2} + h^{(a)}\right)\left(\sin\left(\beta\left(\frac{h_0}{2} + h^{(a)}\right)\right)\right) - \left(\frac{h_0}{2}\right)\sin\left(\beta\frac{h_0}{2}\right)\right]$$

$$A_5 = \frac{1}{2} e_{31} b \left[\frac{1}{\beta}\left(\cos\left(-\beta\frac{h_0}{2}\right) - \cos\left(\beta\left(-\frac{h_0}{2} - h^{(s)}\right)\right)\right) - \left(\frac{h_0}{2}\right)\sin\left(-\beta\frac{h_0}{2}\right) + \left(\frac{h_0}{2} + h^{(s)}\right)\left(\sin\left(\beta\left(-\frac{h_0}{2} - h^{(s)}\right)\right)\right)\right]$$

$$A_6 = \left(-\rho^{(a)} I^{(a)} - \rho^{(S)} I^{(S)} - \rho^{(b)} I^{(b)}\right)$$

$$A_7 = \left(\rho^{(a)} A^{(a)} + \rho^{(s)} A^{(s)} + \rho^{(b)} A^{(b)}\right)$$

$$A_8 = \frac{1}{2} e_{31} b h^{(a)}$$

$$A_9 = -\frac{1}{2} e_{33} \beta b \left[\cos\left(\beta\left(\frac{h_0}{2} + h^{(a)}\right)\right) - \cos\left(\beta\frac{h_0}{2}\right)\right]$$

$$A_{10} = \frac{1}{2} e_{31} b h^{(s)}$$

$$A_{11} = -\frac{1}{2} e_{33} \beta b \left[\cos\left(-\beta\frac{h_0}{2}\right) - \cos\left(\beta\left(-\frac{h_0}{2} - h^{(S)}\right)\right)\right]$$

$$A_{12} = \mu^{(s)} l_2^2 A^{(s)}$$

$$A_{13} = \mu^{(a)} l_2^2 A^{(a)}$$

$$A_{14} = \mu^{(b)} l_2^2 A^{(b)}$$

$$A_{15} = 2\mu^{(b)} l_0^2 A^{(b)}$$

$$A_{16} = 2\mu^{(a)} l_0^2 A^{(a)}$$

$$A_{17} = 2\mu^{(s)} l_0^2 A^{(s)}$$

$$A_{18} = \frac{8}{15} \mu^{(b)} l_1^2 A^{(b)}$$

$$A_{19} = \frac{8}{15} \mu^{(a)} l_1^2 A^{(a)}$$

$$A_{20} = \frac{8}{15} \mu^{(s)} l_1^2 A^{(s)}$$

$$A_{21} = -2\mu^{(b)} l_0^2 I^{(b)}$$

$$A_{22} = -2\mu^{(a)} l_0^2 I^{(a)}$$

$$A_{23} = -2\mu^{(s)} l_0^2 I^{(s)}$$

$$A_{24} = -\frac{4}{5}\mu^{(b)} l_1^2 I^{(b)}$$

$$A_{25} = -\frac{4}{5}\mu^{(a)} l_1^2 I^{(a)}$$

$$A_{26} = -\frac{4}{5}\mu^{(s)} l_1^2 I^{(s)} \tag{C-1}$$

$$B_1^S = E^{s(a)}\frac{h^2}{4}b \tag{C-2}$$

$$B_2^S = \frac{1}{2}e_{31}^{s(a)} b\beta\left(-\frac{h}{2}\right)\cos(-\frac{h}{2}\beta)$$

$$B_3^S = 2\tau^{s(a)} b$$

$$B_4^S = 2\left(-\frac{h_0^3}{24}+\frac{h^3}{24}\right)E^{s(a)}$$

$$B_5^S = e_{31}^{s(a)}\left[\frac{1}{\beta}\cos\left(-\frac{h_0}{2}\beta\right)-\frac{h_0}{2}\sin\left(-\beta\frac{h_0}{2}\right)-\frac{1}{\beta}\cos\left(-\frac{h}{2}\beta\right)+\frac{h}{2}\sin\left(-\beta\frac{h}{2}\right)\right]$$

$$B_6^S = E^{s(a)}\frac{h_0^2}{4}b$$

$$B_7^S = \frac{1}{2}e_{31}^{s(a)}(b)\left(-\frac{h_0}{2}\right)\beta\cos\left(-\frac{h_0}{2}\beta\right)$$

$$B_8^S = E^{s(b)} b\frac{h_0^2}{2}+E^{s(b)}\frac{h_0^3}{6}$$

$$B_9^S = 2\tau^{s(b)} b$$

$$B_{10}^S = E^{s(s)}\frac{h^2}{4}b$$

$$B_{11}^S = \frac{1}{2}e_{31}^{s(s)} b\beta\left(\frac{h}{2}\right)\cos\left(\frac{h}{2}\beta\right)$$

$$B_{12}^S = 2\tau^{s(s)} b$$

$$B_{13}^S = e_{31}^{s(s)}\left[\frac{1}{\beta}\cos\left(\frac{h}{2}\beta\right)+\frac{h}{2}\sin\left(\beta\frac{h}{2}\right)-\frac{1}{\beta}\cos\left(\frac{h_0}{2}\beta\right)-\frac{h_0}{2}\sin\left(\beta\frac{h_0}{2}\right)\right]$$

$$B_{14}^S = 2(-\frac{h^3}{24}+\frac{h_0^3}{24})E^{s(s)}$$

$$B_{15}^S = E^{s(s)}\frac{h_0^2}{4}b$$

$$B_{16}^S = \frac{1}{2}e_{31}^{s(s)} b\left(\frac{h_0}{2}\right)\beta\cos\left(\frac{h_0}{2}\beta\right)$$

References

[1] Oveissi S, Eftekhari SA, Toghraie D. Longitudinal vibration and instabilities of carbon nanotubes conveying fluid considering size effects of nanoflow and nanostructure. Physica E Low Dimens. Syst. Nanostruct. 2016;83:164–73. https://doi.org/10.1016/j.physe.2016.05.010.

[2] Oveissi S, Toghraie D, Eftekhari SA. Longitudinal vibration and stability analysis of carbon nanotubes conveying viscous fluid. Physica E Low Dimens. Syst. Nanostruct. 2016;83:275–83. https://doi.org/10.1016/j.physe.2016.05.004.

[3] Chen J, Khaje Khabaz M, Mehdi Ghasemian M, Altalbawy FMA, Turki Jalil A, Ali Eftekhari S, et al. Albahash, Transverse vibration analysis of double-walled carbon nanotubes in an elastic medium under temperature gradients and electrical fields based on nonlocal Reddy beam theory. Mater Sci Eng: B 2023;291:116220.

[4] C. Lin , J. Zhou , Q. Lu , M.K. Khabaz , A.K. Andani , M. Al-Yasiri , et al. , Thermal conductivity prediction of WO3-CuO-Ag (35: 40: 25)/Water hybrid ternary nanofluid with Artificial Neural Network and back-propagation algorithm, Materials Today Communications, DOI (2023) 106807.

[5] Zhang J, Wang X, Zhou L, Liu G, Adroja DT, da Silva I, et al. A ferrotoroidic candidate with well-separated spin chains. Adv Mater 2022;34:2106728.

[6] Chung KL, Tian H, Wang S, Feng B, Lai G. Miniaturization of microwave planar circuits using composite microstrip/coplanar-waveguide transmission lines. Alex Eng J 2022;61:8933–42.

[7] Zhang X, Tang Y, Zhang F, Lee CS. A novel aluminum–graphite dual-ion battery. Adv Energy Mater 2016;6:1502588.

[8] Wang M, Jiang C, Zhang S, Song X, Tang Y, Cheng H-M. Reversible calcium alloying enables a practical room-temperature rechargeable calcium-ion battery with a high discharge voltage. Nat Chem 2018;10:667–72.

[9] Gao Y, Doppelbauer M, Ou J, Qu R. Design of a double-side flux modulation permanent magnet machine for servo application. IEEE J Emerg Sel Top Power Electron 2021;10:1671–82.

[10] Wu Z, Huang B, Fan J, Chen H. Homotopy based stochastic finite element model updating with correlated static measurement data. Measurement 2023;210:112512.

[11] Cao J, Bu F, Wang J, Bao C, Chen W, Dai K. Reconstruction of full-field dynamic responses for large-scale structures using optimal sensor placement. J Sound Vib 2023;554:117693.

[12] Wang Y-Y, Lou M, Wang Y, Wu W-G, Yang F. Stochastic failure analysis of reinforced thermoplastic pipes under axial loading and internal pressure. China Ocean Eng 2022;36:614–28.

[13] Zhang Y, Hammoodi KA, Sajadi SM, Li Z, Jasim DJ, Nasajpour-Esfahani N, et al. Obtaining an accurate prediction model for viscosity of a new nano-lubricant containing multi-walled carbon nanotube-titanium dioxide nanoparticles with oil SAE50. Tribology Int 2024;191:109185.

[14] Song J, Mingotti A, Zhang J, Peretto L, Wen H. Fast iterative-interpolated DFT phasor estimator considering out-of-band interference. IEEE Trans Instrum Meas 2022;71:1–14.

[15] Bai X, He Y, Xu M. Low-thrust reconfiguration strategy and optimization for formation flying using Jordan normal form. IEEE Trans Aerosp Electron Syst 2021;57:3279–95.

[16] Zhu Z, Liu Y, Gou G, Gao W, Chen J. Effect of heat input on interfacial characterization of the butter joint of hot-rolling CP-Ti/Q235 bimetallic sheets by Laser+ CMT. Sci Rep 2021;11:10020.

[17] Zhu Q, Chen J, Gou G, Chen H, Li P. Ameliorated longitudinal critically refracted—Attenuation velocity method for welding residual stress measurement. J Mater Process Technol 2017;246:267–75.

[18] Zhang H, Xiang X, Huang B, Wu Z, Chen H. Static homotopy response analysis of structure with random variables of arbitrary distributions by minimizing stochastic residual error. Comput Struct 2023;288:107153.

[19] Esfe MH, Eftekhari SA, Hekmatifar M, Toghraie D. A well-trained artificial neural network for predicting the rheological behavior of MWCNT–Al2O3 (30–70%)/oil SAE40 hybrid nanofluid. Sci Rep 2021;11:1–11.

[20] Fu Z, Yang B, Shan M, Li T, Zhu Z, Ma C, et al. Hydrogen embrittlement behavior of SUS301L-MT stainless steel laser-arc hybrid welded joint localized zones. Corros Sci 2020;164:108337.

[21] Korayem M, Homayooni A. The size-dependent analysis of multilayer micro-cantilever plate with piezoelectric layer incorporated voltage effect based on a modified couple stress theory. Eur J Mech-A/Solids 2017;61:59–72.

[22] Bakhshi Khaniki H, Hosseini-Hashemi S. The size-dependent analysis of multilayered microbridge systems under a moving load/mass based on the modified couple stress theory. Eur Phys J 2017;132:1–18.

[23] Hashemi SH, Khaniki HB. Dynamic behavior of multi-layered viscoelastic nanobeam system embedded in a viscoelastic medium with a moving nanoparticle. J Mech 2017;33:559–75.

[24] Arshid E, Amir S, Loghman A. On the vibrations of FG GNPs-RPN annular plates with piezoelectric/metallic coatings on Kerr elastic substrate considering size dependency and surface stress effects. Acta Mech 2023:1–42.

[25] Arshid E, Khorasani M, Soleimani-Javid Z, Amir S, Tounsi A. Porosity-dependent vibration analysis of FG microplates embedded by polymeric nanocomposite patches considering hygrothermal effect via an innovative plate theory. Eng Comput 2021:1–22.

[26] Kabir M, Kazari H, Ozevin D. Piezoelectric MEMS acoustic emission sensors, Sensors and Actuators A: Physical 2018;279:53–64.

[27] Wang K, Wang B, Xu M, Yu A. Influences of surface and interface energies on the nonlinear vibration of laminated nanoscale plates. Compos Struct 2018;183:423–33.

[28] Wang K, Zeng S, Wang B. Large amplitude free vibration of electrically actuated nanobeams with surface energy and thermal effects. Int J Mech Sci 2017;131:227–33.

[29] Chaudhari VK, Lal A. Nonlinear free vibration analysis of elastically supported nanotube-reinforced composite beam in thermal environment. Procedia Eng 2016;144:928–35.

[30] Cao J, Quek S-T, Xiong H, Yang Z. Comparison of Constrained Unscented and Cubature Kalman Filters for Nonlinear System Parameter Identification. J Eng Mech 2023;149:04023088.

[31] Hu Z, He G, Zhang X, Huang T, Li H, Zhang Y, et al. Impact behavior of nylon kernmantle ropes for high-altitude fall protection. J Eng Fibers Fabr 2023;18.15589250231167401.

[32] Zheng Y-f, Qu D-y, Liu L-c, Chen C-p. Size-dependent nonlinear bending analysis of nonlocal magneto-electro-elastic laminated nanobeams resting on elastic foundation. Int J Non-Linear Mech 2023;148:104255.

[33] Zhang X, Wang S, Liu H, Cui J, Liu C, Meng X. Assessing the impact of inertial load on the buckling behavior of piles with large slenderness ratios in liquefiable deposits. Soil Dyn Earthq Eng 2024;176:108322.

[34] Du S, Xie H, Yin J, Fang T, Zhang S, Sun Y, et al. Competition Pathways of Energy Relaxation of Hot Electrons through Coupling with Optical, Surface, and Acoustic Phonons. J Phys Chem C 2023;127:1929–36.

[35] Arefi M, Zenkour AM. Vibration and bending analysis of a sandwich microbeam with two integrated piezo-magnetic face-sheets. Compos Struct 2017;159:479–90.

[36] Wang Y, Lou M, Wang Y, Fan C, Tian C, Qi X. Experimental investigation of the effect of rotation rate and current speed on the dynamic response of riserless rotating drill string. Ocean Eng 2023;280:114542.

[37] Gohari S, Sharifi S, Vrcelj Z. New explicit solution for static shape control of smart laminated cantilever piezo-composite-hybrid plates/beams under thermo-electro-mechanical loads using piezoelectric actuators. Compos Struct 2016;145:89–112.

[38] Zhang Y, He X, Cong X, Wang Q, Yi H, Li S, et al. Enhanced energy storage performance of polyethersulfone-based dielectric composite via regulating heat treatment and filling phase. J Alloy Compd 2023;960:170539.

[39] Wu Q, Yao M, Niu Y. Nonplanar free and forced vibrations of an imperfect nanobeam employing nonlocal strain gradient theory. Commun Nonlinear Sci Numer Simul 2022;114:106692.

[40] Moradi A, Shirazi KH, Keshavarz M, Falehi AD, Moradi M. Smart piezoelectric patch in non-linear beam: design, vibration control and optimal location. Trans Inst Meas Control 2014;36:131–44.

[41] Nojoumian M, Shirazi MJ, Salarieh H. Boundary control of a marine riser pipe conveying fluid, ASME International Mechanical Engineering Congress and Exposition. American Society of Mechanical Engineers. 2014. V04AT04A013.

[42] Nguyen-Quang K, Dang-Trung H, Ho-Huu V, Luong-Van H, Nguyen-Thoi T. Analysis and control of FGM plates integrated with piezoelectric sensors and actuators using cell-based smoothed discrete shear gap method (CS-DSG3). Compos Struct 2017;165:115–29.

[43] Ghorbanpour Arani A, Khoddami Maraghi Z, Khani H. Arani, Vibration control of magnetostrictive plate under multi-physical loads via trigonometric higher order shear deformation theory. J Vib Control 2017;23:3057–70.

[44] AkhavanAlavi S, Mohammadimehr M, Edjtahed S. Active control of micro Reddy beam integrated with functionally graded nanocomposite sensor and actuator based on linear quadratic regulator method. Eur J Mech-A/Solids 2019;74:449–61.

[45] Vatankhah R, Asemani MH. Output feedback control of piezoelectrically actuated non-classical micro-beams using TS fuzzy model. J Frankl Inst 2017;354:1042–65.

[46] Vakilzadeh M, Vatankhah R, Eghtesad M. Vibration control of micro-scale structures using their reduced second order bilinear models based on multi-moment matching criteria. Appl Math Model 2020;78:287–96.

[47] Khabaz MK, Eftekhari SA, Toghraie D. Vibration and dynamic analysis of a cantilever sandwich microbeam integrated with piezoelectric layers based on strain gradient theory and surface effects. Appl Math Comput 2022;419.

[48] Khajekhabaz M, Eftekhari A, Hashemian M. Free vibration analysis of sandwich micro beam with piezoelectric based on modified couple stress theory and surface effects. J Simul Anal Nov Technol Mech Eng 2018;10:33–48.

[49] Wang L, Zhao Y, Liu J, Kriging-based A. decoupled non-probability reliability-based design optimization scheme for piezoelectric PID control systems. Mech Syst Signal Process 2023;203:110714.

[50] Eftekhari SA, Hashemian M, Toghraie D. Optimal vibration control of multi-layer micro-beams actuated by piezoelectric layer based on modified couple stress and surface stress elasticity theories. Phys A: Stat Mech Appl 2020;546:123998.

[51] Hu G, Ying S, Qi H, Yu L, Li G. Design, analysis and optimization of a hybrid fluid flow magnetorheological damper based on multiphysics coupling model. Mech Syst Signal Process 2023;205:110877.

[52] Zhang C. The active rotary inertia driver system for flutter vibration control of bridges and various promising applications. Sci China Technol Sci 2023;66:390–405.

[53] Sun T, Peng L, Ji X, Li X. A half-cycle negative-stiffness damping model and device development. Struct Control Health Monit 2023;2023.

[54] M. Khaje Khabaz S.A. Eftekhari M. Hashemian Vib Anal Control cantilever Micro-beam Integr piezoelectric Actuator Sens layers considering Surf Eff 9 2018 34 45.

[55] Zhang M, Jiang X, Arefi M. Dynamic formulation of a sandwich microshell considering modified couple stress and thickness-stretching. Eur Phys J 2023;138:227.

[56] Muc A, Kędziora P, Stawiarski A. Buckling enhancement of laminated composite structures partially covered by piezoelectric actuators. Eur J Mech - A/Solids 2019;73:112–25.

[57] C. Luo , L. Wang , Y. Xie , B. Chen , A new conjugate gradient method for moving force identification of vehicle–bridge system, Journal of Vibration Engineering & Technologies, DOI (2022) 1–18.
[58] Ansari R, Ashrafi M, Hosseinzadeh S. Vibration characteristics of piezoelectric microbeams based on the modified couple stress theory. Shock Vib 2014;2014.
[59] Li Y, Feng W. Microstructure-dependent piezoelectric beam based on modified strain gradient theory. Smart Mater Struct 2014;23:095004.
[60] Eftekhari SA, Toghraie D. Vibration and dynamic analysis of a cantilever sandwich microbeam integrated with piezoelectric layers based on strain gradient theory and surface effects. Appl Math Comput 2022;419:126867.
[61] Keivani M, Koochi A, Kanani A, Mardaneh MR, Sedighi HM, Abadyan M. Using strain gradient elasticity in conjunction with Gurtin–Murdoch theory for modeling the coupled effects of surface and size phenomena on the instability of narrow nano-switch. Proc Inst Mech Eng, Part C: J Mech Eng Sci 2017;231:3277–88.
[62] Arani AG, Abdollahian M, Kolahchi R. Nonlinear vibration of a nanobeam elastically bonded with a piezoelectric nanobeam via strain gradient theory. Int J Mech Sci 2015;100:32–40.
[63] Sedighi HM. Size-dependent dynamic pull-in instability of vibrating electrically actuated microbeams based on the strain gradient elasticity theory. Acta Astronaut 2014;95:111–23.
[64] S.A.M. Hejazi , A. Feyzpour , M. Khaje khabaz , A. Eslami , M. Fouladgar , S.A. Eftekhari , et al. , Numerical Investigation of Rigidity and Flexibility Parameters Effect on Superstructure Foundation Behavior Using Three-Dimensional Finite Element Method, Case Studies in Construction Materials, DOI https://doi.org/10.1016/j.cscm.2023.e01867(2023) e01867.
[65] Oveissi S, Toghraie D, Eftekhari SA, Chamkha AJ. Instabilities of SWCNT conveying laminar, incompressible and viscous fluid flow: effects of Knudsen number, the Winkler, the Pasternak elastic and the viscoelastic medium. Int J Numer Methods Heat Fluid Flow 2019.
[66] Rostami SAL, Kolahdooz A, Zhang J. Robust topology optimization under material and loading uncertainties using an evolutionary structural extended finite element method. Eng Anal Bound Elem 2021;133:61–70.
[67] Farrokhian A, Salmani-Tehrani M. Vibration and damping analysis of smart sandwich nanotubes using surface-visco-piezo-elasticity theory for various boundary conditions. Eng Anal Bound Elem 2022;135:337–58.
[68] Shafiei N, Mousavi A, Ghadiri M. Vibration behavior of a rotating non-uniform FG microbeam based on the modified couple stress theory and GDQEM. Compos Struct 2016;149:157–69.
[69] Xia J, Khabaz MK, Patra I, Khalid I, Alvarez JRN, Rahmanian A, et al. Using feed-forward perceptron Artificial Neural Network (ANN) model to determine the rolling force, power and slip of the tandem cold rolling. ISA Trans 2022.
[70] Z. Babajamali , M.K. khabaz , F. Aghadavoudi , F. Farhatnia , S.A. Eftekhari , D. Toghraie , Pareto multi-objective optimization of tandem cold rolling settings for reductions and inter stand tensions using NSGA-II, ISA Transactions, DOI https://doi.org/10.1016/j.isatra.2022.04.002(2022).
[71] Keleshteri M, Jelovica J. Beam theory reformulation to implement various boundary conditions for generalized differential quadrature method. Eng Struct 2022;252:113666.
[72] Pirmoradian M, Naeeni HA, Firouzbakht M, Toghraie D, khabaz MK, Darabi R. Finite element analysis and experimental evaluation on stress distribution and sensitivity of dental implants to assess optimum length and thread pitch. Comput Methods Prog Biomed 2020;187:105258.
[73] Alam MN. Active vibration control of a piezoelectric beam using PID controller: Experimental study. Lat Am J Solids Struct 2012;9:657–73.
[74] Mirghaffari A, Rahmani B. Active vibration control of carbon nanotube reinforced composite beams. Trans Inst Meas Control 2017;39:1851–63.
[75] M. Yang, Y. Wang, X. Xiao, Y. Li, A. Robust Damping Control for Virtual Synchronous Generators Based on Energy Reshaping, IEEE Transactions on Energy Conversion, DOI (2023).
[76] Yang R, Kai Y. Dynamical properties, modulation instability analysis and chaotic behaviors to the nonlinear coupled Schrödinger equation in fiber Bragg gratings. Mod Phys Lett B 2024;38:2350239.
[77] P. Wang , X. Wu , X. He , Vibration-Theoretic Approach to Vulnerability Analysis of Nonlinear Vehicle Platoons, IEEE Transactions on Intelligent Transportation Systems, DOI (2023).
[78] Talebitooti R, Daneshjoo K, Jafari S. Optimal control of laminated plate integrated with piezoelectric sensor and actuator considering TSDT and meshfree method. Eur J Mech-A/Solids 2016;55:199–211.
[79] Lu Z-Q, Wu D, Ding H, Chen L-Q. Vibration isolation and energy harvesting integrated in a Stewart platform with high static and low dynamic stiffness. Appl Math Model 2021;89:249–67.
[80] Y. Shi , X. Hou , Z. Na , J. Zhou , N. Yu , S. Liu , , , et al. , Bio-inspired attachment mechanism of dynastes Hercules: vertical climbing for on-orbit assembly legged robots, Journal of Bionic Engineering, DOI (2023) 1–12.
[81] Song F, Liu Y, Shen D, Li L, Tan J. Learning control for motion coordination in wafer scanners: Toward gain adaptation. IEEE Trans Ind Electron 2022;69:13428–38.
[82] Hao R, Lu Z, Ding H, Chen L-Q. Shock isolation of an orthogonal six-DOFs platform with high-static-low-dynamic stiffness. J Appl Mech 2023;90:111004.
[83] H. Kwakernaak , R. Sivan , Linear optimal control systems, Wiley-interscience New York1972.
[84] Wang L, Zhou Z, Liu J. Interval-based optimal trajectory tracking control method for manipulators with clearance considering time-dependent reliability constraints. Aerosp Sci Technol 2022;128:107745.
[85] Z. Feng , J. Zhu , R. Allen , Design of LQI control systems with stable inner loops, Journal of Shanghai Jiaotong University (Science), vol. E, DOI (2007).
[86] Boyer MD, Barton J, Schuster E, Luce TC, Ferron JR, Walker ML, et al. First-principles-driven model-based current profile control for the DIII-D tokamak via LQI optimal control. Plasma Phys Control Fusion 2013;55:105007.
[87] Hao R-B, Lu Z-Q, Ding H, Chen L-Q. Orthogonal six-DOFs vibration isolation with tunable high-static-low-dynamic stiffness: experiment and analysis. Int J Mech Sci 2022;222:107237.
[88] Kong S, Zhou S, Nie Z, Wang K. Static and dynamic analysis of micro beams based on strain gradient elasticity theory. Int J Eng Sci 2009;47:487–98.
[89] Hamilton J, Wolfer W. Theories of surface elasticity for nanoscale objects. Surf Sci 2009;603:1284–91.